Journal of Alloys and Compounds 489 (2010) 195–201

Contents lists available at ScienceDirect

Journal of Alloys and Compounds

journal homepage: www.elsevier.com/locate/jallcom

High temperature oxidation characteristics of Nb–10W–*X*Cr alloys

Maria del Pilar Moricca, S.K. Varma*

Department of Metallurgical and Materials Engineering, The University of Texas at El Paso, 500 W. University, El Paso, TX 79968-0520, United States

ARTICLE INFO

Article history:
Received 29 July 2009
Received in revised form 8 September 2009
Accepted 9 September 2009
Available online 16 September 2009

Keywords:
Nb–W–Cr
Laves phase
Microstructure
Oxidation
XRD
EDS

ABSTRACT

The effect of Cr content on the microstructure and cyclic oxidation behavior of Nb–10W–XCr alloys with four different compositions has been investigated. Experiments were conducted in air at 900 °C and 1300 °C; the oxidation kinetics have been evaluated in terms of weight change per unit area with respect to exposure time. Alloy's microstructure consists of Nb solid solution phase regions surrounded by a network of $NbCr_2$ Laves phase. A trend of improvement in oxidation resistance with increase of the intermetallic phase is observed at 1300 °C and oxidation kinetics follow a parabolic behavior. At 900 °C, alloys with higher Cr content exhibit higher oxidation rates than alloys with lower Cr content. The oxidation products are a mixture of $CrNbO_4$, and Nb_2O_5 and the amount of each oxide present in the mixture is related to the intermetallic phase content. Results delineate the influence of microstructure and composition on the oxidation mechanisms of these alloys that represent a promising base for high-temperature intermetallic alloy development.

1. Introduction

Considerable efforts have been devoted to enhance the capabilities of high temperature materials in order to develop higher efficiency engines and advanced aerospace systems. Extensive investigations aimed to improve the oxidation resistance of Nb alloys have been performed. Initial studies of binary alloys of niobium with titanium, chromium, vanadium, molybdenum and certain other elements showed that these alloys exhibit enhanced oxidation resistance than pure niobium, but not sufficiently high to be used as oxidation-resistant materials [1]. Subsequent studies concentrated on the use of Al additions to induce the formation of a protective alumina scale. Although a protective layer of oxide was formed, the resulting alloys exhibit lower melting points and increased brittleness [2–4].

Recent studies are oriented towards the development of niobium systems with Al, Cr, Ge, Hf, Si, and Ti additions; often referred to as refractory metal-intermetallic composites (RMICs). These niobium alloys contain multiphase microstructures comprised of silicides, Laves phase and Nb solid solution [5–16]. A multiphase system is expected to provide improved high temperature strength and environmental resistance while retaining fracture toughness at low temperatures.

The multiphase approach has lead to the study of systems that provide a high level of freedom in selecting compositions of the constituent phases in order to obtain a more favorable balance of high temperature strength and good oxidation resistance. Recent studies show that the Nb–Cr–X system (X is a refractory metal) may exhibit such characteristics [17–19]. The results of oxidation resistance in air for Nb–20W–5Cr and Nb–20W–10Cr (composition is in weight percents) have been reported recently [20,21].

Oxidation models for treating the oxidation behavior of two-phase binary alloys have been proposed by Wang et al. [22] and Gesmundo et al. [23,24]. A cyclic oxidation model for multiphase Nb alloys was developed by Chan [2]; this model indicates that the oxidation resistance of two-phase Nb alloys depends on the volume fraction and particle size of the Laves and silicide phases. Understanding the oxidation kinetics of Nb-based alloys and the role of the different phases in the oxidation process is of crucial importance to improve the oxidation resistance of these alloys. This article presents the results of an investigation performed in order to study the effect of the Cr content on the cyclic oxidation behavior of four alloys from the Nb–W–Cr system at 900 °C and 1300 °C.

2. Experimental procedures

2.1. Alloys preparation

The alloys were fabricated by the Ames Laboratory of Iowa State University using arc melting technique. Nb, W, and Cr with a 99.9% minimum purity were melted on a water-cooled copper crucible in an atmosphere of high purity argon gas; the samples were remelted several times to ensure chemical homogeneity. The alloys were cast into ingots with dimensions of 50 mm × 50 mm × 6 mm; final dimensions were obtained using electro-discharge machining (EDM).

The selection of specific alloy compositions has been based on the ternary isothermal sections of Nb–Cr–W diagrams at 1000 °C and 1500 °C [25]. Table 1 presents the nominal compositions of the alloys used for this study.

* Corresponding author. Tel.: +1 915 747 6937; fax: +1 915 747 8036.
E-mail address: skvarma@utep.edu (S.K. Varma).

0925-8388/$ – see front matter © 2009 Elsevier B.V. All rights reserved.
doi:10.1016/j.jallcom.2009.09.051

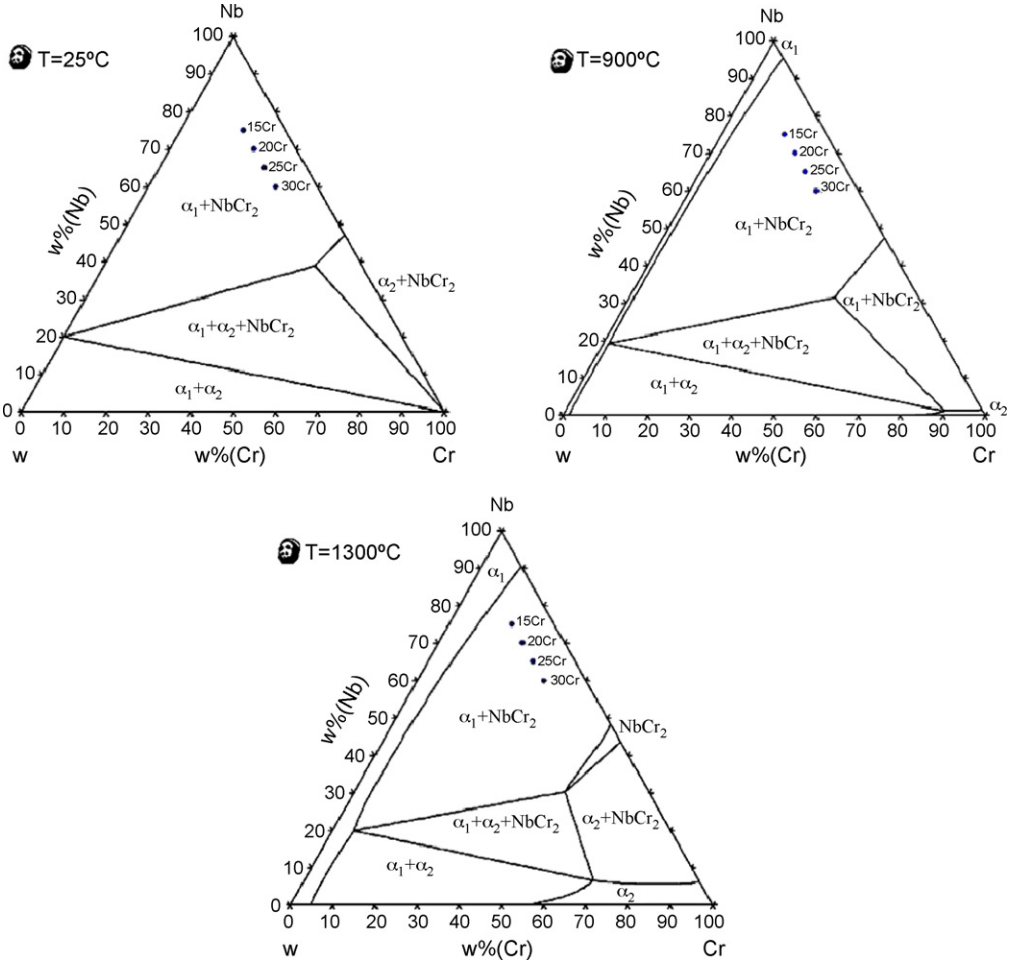

Fig. 1. Isothermal sections at 25 °C, 900 °C, and 1300 °C for the Nb–W–Cr system calculated using Pandat™ 7.0 software [26].

Isothermal sections of the Nb–Cr–W phase diagram at 25 °C, 900 °C, and 1300 °C were calculated using a phase diagram calculation software for multicomponent systems, Pandat™ 7.0 provided by the Computherm LLC [26].

2.2. Alloys characterization

The as-cast samples were prepared by standard sample preparation techniques for metallography. The etchant used was a solution of HF, HNO_3, and HCl in a ratio of 2:1:2 [27].

Microstructure of the alloys was characterized using optical microscopy (OM), scanning electron microscopy (SEM) and energy dispersive X-ray spectroscopy (EDS). Phases of the alloys were identified by X-ray diffraction (XRD).

2.3. Oxidation experiments

The oxidation coupons with dimensions of approximately 4 mm × 4 mm × 3 mm were ground to 600 grit and ultrasonically cleaned in ethanol before exposure. Cyclic oxidation measurements were performed at 900 °C and 1300 °C in a box furnace using a heating rate of 14 °C/min, the specimens were held at the peak temperature for 4 h and then furnace cooled to ambient temperature. The samples were weighed before and after each thermal cycle; this process was repeated for a total oxidation time of 24 h. Weight gain per unit area as a function of the temperature has been used to determine the alloy's oxidation resistance. The oxidation products were characterized by XRD. The surface morphologies of the oxide and the cross-section of the scales were observed and analyzed by SEM and EDS.

Table 1
Nominal composition in weight percent of Nb–Cr–W alloys.

Sample	%Nb	%Cr	%W
15Cr	75	15	10
20Cr	70	20	10
25Cr	65	25	10
30Cr	60	30	10

3. Results

3.1. As cast characterization

The isothermal sections at 25 °C, 900 °C, and 1300 °C from the Nb–W–Cr phase diagram calculated by using Pandat software are presented in Fig. 1. The four alloys analyzed remain in a two phase region consisting of Nb rich solid solution and intermetallic phase $NbCr_2$ through the entire temperature range.

Optical images of 15Cr, 20Cr, 25Cr, and 30Cr alloys in the as-cast condition are presented in Fig. 2. Microstructure of alloys consists of Nb solid solution phase regions (white) and the intermetallic $NbCr_2$ Laves phase (gray), an increase of the intermetallic phase is observed as the Cr content increases.

The EDS analysis on the SEM indicates the locations of Cr and Nb rich regions. The BSE images and X-ray maps presented in Figs. 3 and 4 exhibit the two phase structure for the 15Cr and 30Cr alloys, respectively, in the as cast condition.

Table 2 presents the chemical composition determined by EDS for each alloy in the as-cast condition, as well as the fraction of the $NbCr_2$ phase which was measured using image analysis and the BSE contrast.

The XRD patterns obtained from the as cast structures are shown in Fig. 5. Individual phases and their crystal structures were identified by matching the characteristic XRD peaks against JCPDS files. The peak identification confirms the presence of two phases, Nb

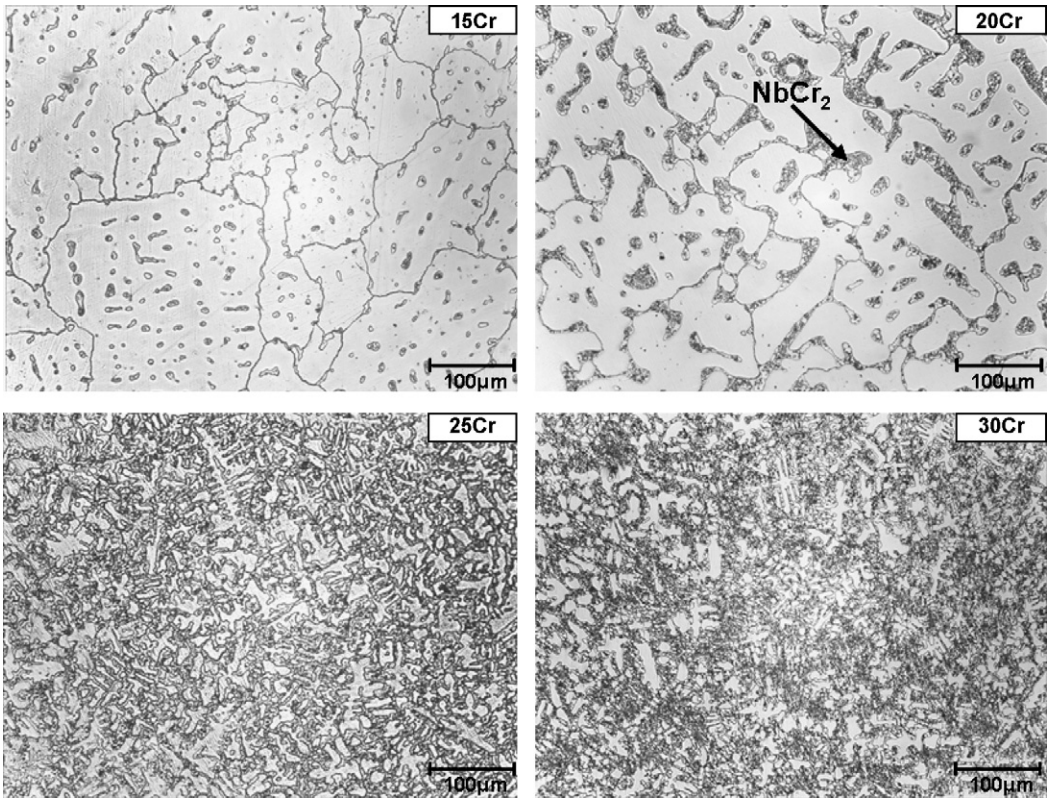

Fig. 2. Optical images of the as-cast microstructure of Nb–W–Cr alloys.

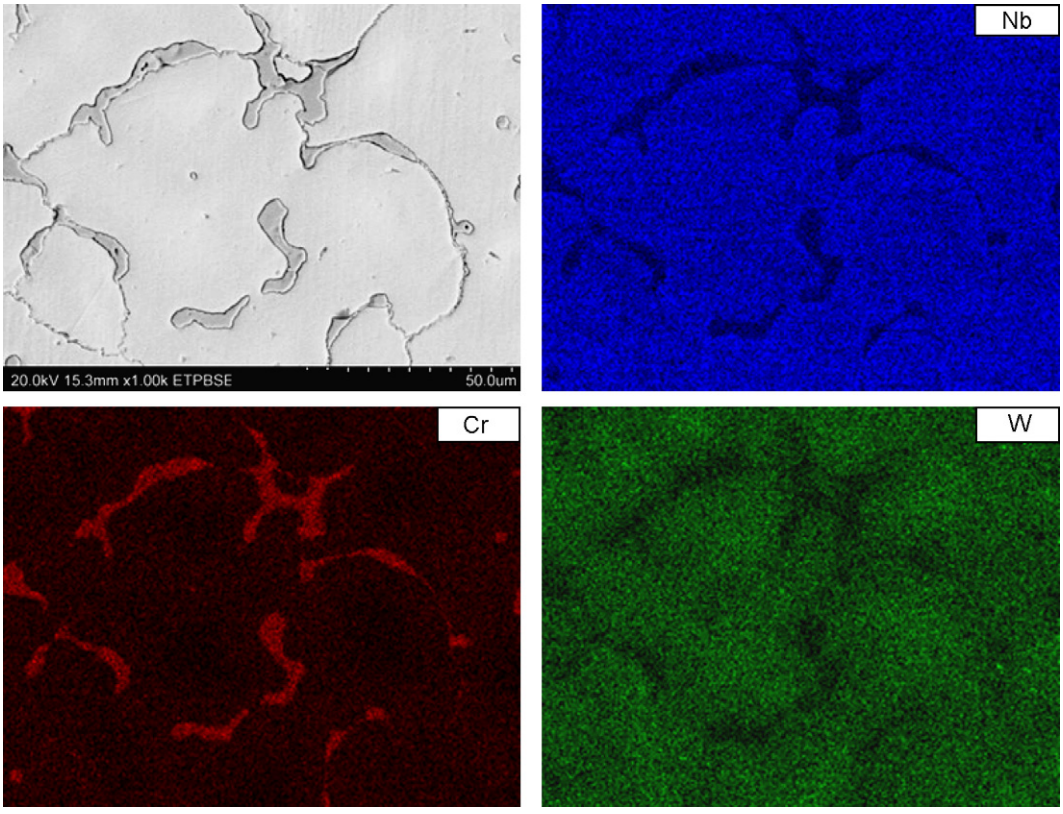

Fig. 3. BSE image and X-ray maps of 15Cr alloy showing Nb, Cr, and W distribution.

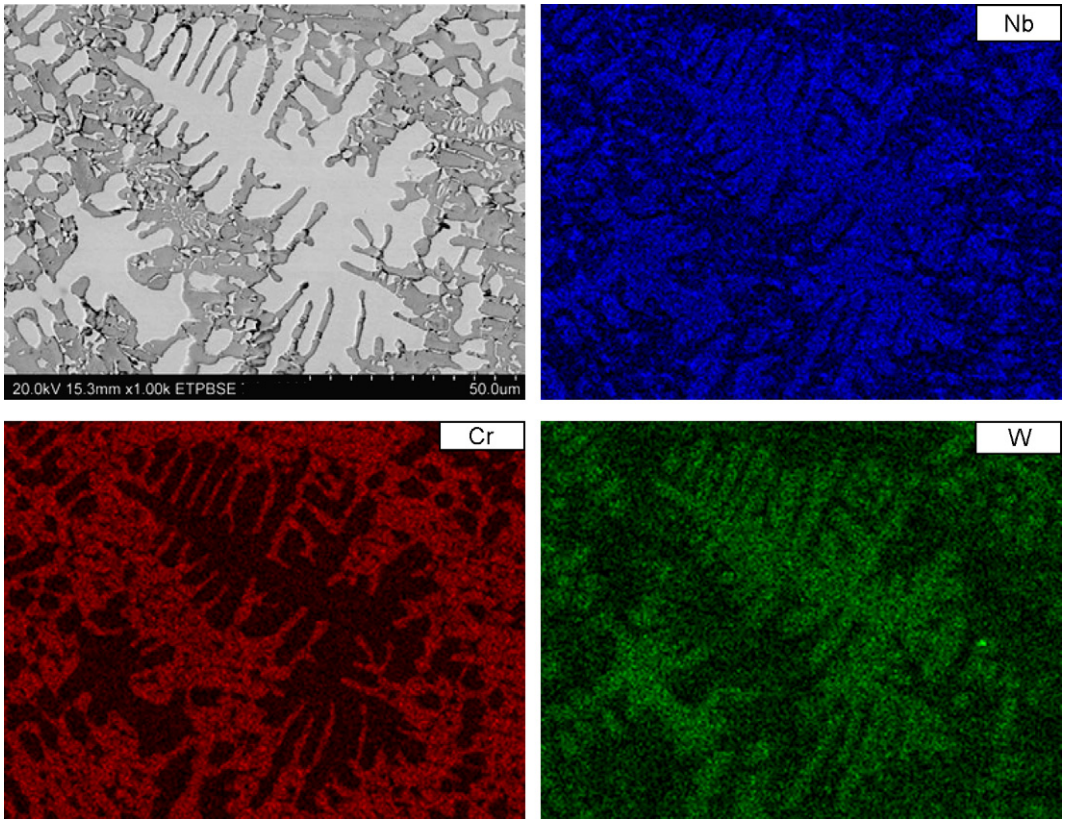

Fig. 4. BSE image and X-ray maps of 30Cr alloy showing Nb, Cr, and W distribution.

solid solution (α) and the cubic type (C15) Laves phase $NbCr_2$. The dashed lines represent the diffraction positions of the pure niobium (JCPDS 34-370). The Nb solid solution peaks in all the as-cast alloys were shifted slightly to the right (higher 2θ values) of the intensity peaks of pure Nb suggesting that the solid solution phase has a reduced lattice parameter compared to pure niobium. Since the atomic radii of pure Nb, Cr, and W are 1.47, 1.28, and 1.41 respectively [28], a smaller lattice parameter can be attributed to the substitutions of Cr and W in the Nb solid solution, considering only the size effect of substitutional atoms.

Table 2
Elemental compositions determined by EDS analysis and area fraction of the $NbCr_2$ phase in the as cast condition.

Alloy	Element (wt%)			$NbCr_2$ phase (area percentage)
	Nb	Cr	W	
15Cr	74.5–76.3	12.4–14.0	10.7–12.4	7.6 ± 0.9
20Cr	69.6–71.9	17.1–18.6	10.7–11.9	18.3 ± 1.2
25Cr	62.4–65.7	24.2–26.6	8.9–11.8	43.0 ± 0.8
30Cr	60.9–62.4	28.2–30.3	8.2–9.7	56.7 ± 0.9

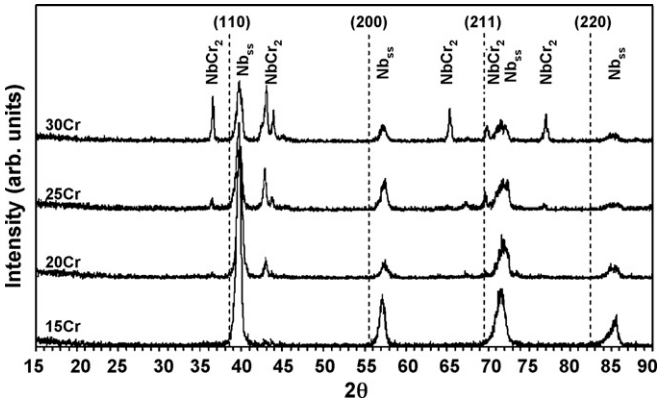

Fig. 5. XRD patterns of 15, 20, 25, and 30Cr alloys in the as cast condition.

3.2. Oxidation behavior

The oxidation rates of all the alloys were measured at 900 °C and 1300 °C in static air. Fig. 6 shows the weight gain per unit area as a function of the exposure time at 1300 °C for the alloys 15Cr, 20Cr, 25Cr, and 30Cr. The oxidation behavior of all the alloys follows a parabolic law at this temperature; the time at which the oxidation rate stabilizes depends on the alloy composition. Preferential attack of the Nb solid solution phase was observed in all the oxidized alloys. The alloys with higher area fractions of Laves phase exhibited better oxidation resistance at 1300 °C, the weight gain per unit area of the 15Cr alloy is almost 3 times that of 30Cr,

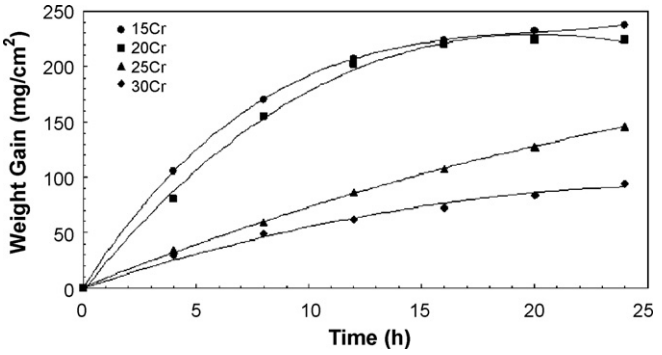

Fig. 6. Cyclic oxidation curves for samples 15Cr, 20Cr, 25Cr, and 30Cr at 1300 °C.

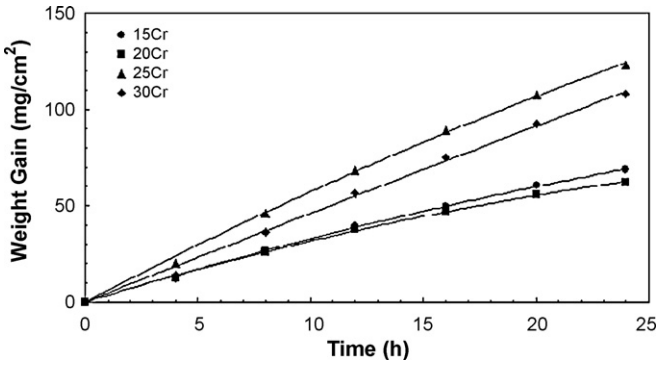

Fig. 7. Cyclic oxidation curves for samples 15Cr, 20Cr, 25Cr, and 30Cr at 900 °C.

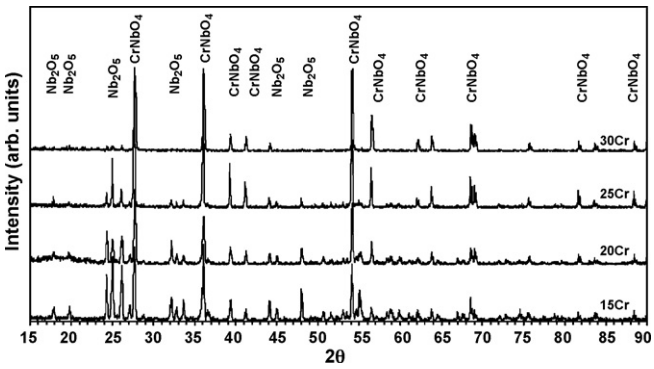

Fig. 8. XRD pattern of the oxidation products obtained from the 4 alloys after 24 h of cyclic exposure at 1300 °C.

delineating the relationship between the oxidation resistance and the fraction of intermetallic phase in the alloy. This behavior is in agreement with the results reported for niobium-based alloys in the literature [2,6,11].

The large difference in weight gain per unit area between alloys 20Cr and 25Cr and the small difference between alloys 25Cr and 30Cr suggest the existence of a limit concerning the effectiveness of the Cr in improving oxidation resistance of these alloys.

Contrary to the behavior observed at 1300 °C, the samples with higher Cr content showed poor oxidation resistance at 900 °C, as shown in Fig. 7. The 30Cr alloy exhibits a weight gain similar to the gain obtained at 1300 °C in spite of a temperature difference of 400 °C. 15Cr and 20Cr alloys exhibit near identical oxidation behavior at the initial oxidation stage (up to 12 h). The oxidation rate of 25Cr and 30Cr alloys remains constant with time suggesting that the oxidation kinetics are rather linear than parabolic and the oxide scale formed is porous and spalls off easily.

The oxidation behavior of samples with 15% Cr is more sensitive to temperature changes when compared to samples with 30% of Cr, which maintain a smaller range of weight change per unit area between both temperatures. The difference between the weight change per unit area values at 900 °C and 1300 °C is about 168 mg/cm^2 for 15Cr alloy while this difference is only 14 mg/cm^2 in the case of 30Cr alloy.

The parabolic rate constants for oxidation tests are listed in Table 3. The parabolic oxidation rate constants (k_p) were calculated by least-square, linear-regression analysis of the mass gain per unit surface ($\Delta m/A$) and the exposure time (t):

$$\left(\frac{\Delta m}{A}\right)^2 = k_p t \quad (1)$$

At 900 °C the alloys 25Cr and 30Cr follow a linear behavior rather than a parabolic which is consistent with the higher oxidation rate (Fig. 7) and the easy spallation of the oxide scale. The oxidation kinetics follow a parabolic behavior at 1300 °C for the four analyzed alloys; the addition of 30% of Cr resulted in the significant reduction of the parabolic oxidation rate.

Table 3
Values of parabolic rate constants (k_p) and correlation coefficients corresponding to cyclic exposure at 900 °C and 1300 °C.

Temperature	Alloy	Time span (h)	k_p (mg^2 cm^{-4} h^{-1})
900	15Cr	0–24	172.4
	20Cr	0–24	146.5
	25Cr	0–24	–
	30Cr	0–24	–
1300	15Cr	0–20	3021.4
	20Cr	0–20	2826.8
	25Cr	0–24	784.7
	30Cr	0–24	348.5

3.3. Oxide scale characterization

The oxidation products of the different alloys were identified by XRD. Fig. 8 presents the XRD patterns obtained from the oxidation products of 15Cr, 20Cr, 25Cr, and 30Cr alloys after 24 h of cyclic exposure at 1300 °C. The products are a mixture of $CrNbO_4$, and Nb_2O_5. As the Cr concentration increases the intensity of the Nb_2O_5 peaks decreases, thus $CrNbO_4$ is the predominant oxide in 30Cr alloy. Oxidation products observed are consistent with those reported for Nb alloys and $NbCr_2$ in the literature [4–7,15,21].

A comparison of the diffraction patterns of the scale formed at 900 °C on 15Cr and 30Cr alloys is presented in Fig. 9. The scale formed on sample 30Cr at 900 °C is a mixture of $CrNbO_4$ and Nb_2O_5, the peak intensity implies that $CrNbO_4$ is the main constituent. As temperature increases the intensity of the Nb_2O_5 decreases and at 1300 °C only the $CrNbO_4$ can be identified. The change in the oxidation products composition is consistent with the oxidation kinetics change observed for sample 30Cr. The oxidation products obtained from 15Cr alloy are a mixture of $CrNbO_4$ and Nb_2O_5 for both temperatures.

The oxide–metal interface images of samples 15Cr and 30Cr oxidized at 900 °C for 24 h are presented in Fig. 10. The oxide scale of sample 15Cr is a combination of Nb_2O_5 and $CrNbO_4$, although some fragmentation of the oxide is observed at the external layers, the alloy does not exhibit crack formation at the interface. Sample 30Cr (Fig. 10(a)) presents numerous microcracks around the perimeter of the sample which causes alloy fragmentation before the complete oxidation of the phases. The formation of these microcracks causes accelerated oxidation and powder formation. These results suggest that the lower oxidation resistance observed in 25Cr and 30Cr alloys at 900 °C is attributed to the severe cracking of the inter-

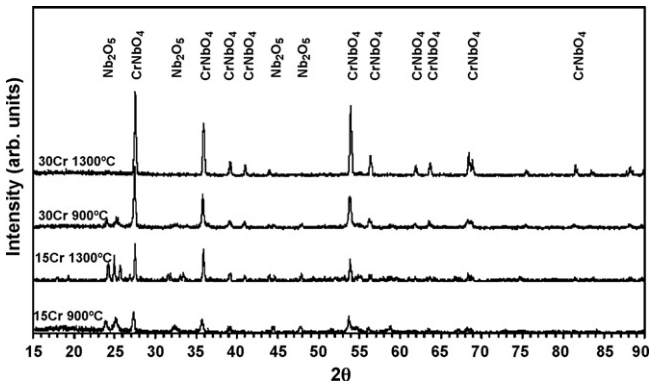

Fig. 9. Comparison of the XRD patterns from oxidation products of samples 15Cr 30Cr after cyclic oxidation (6 cycles) at 900° and 1300 °C for a total of 24 h.

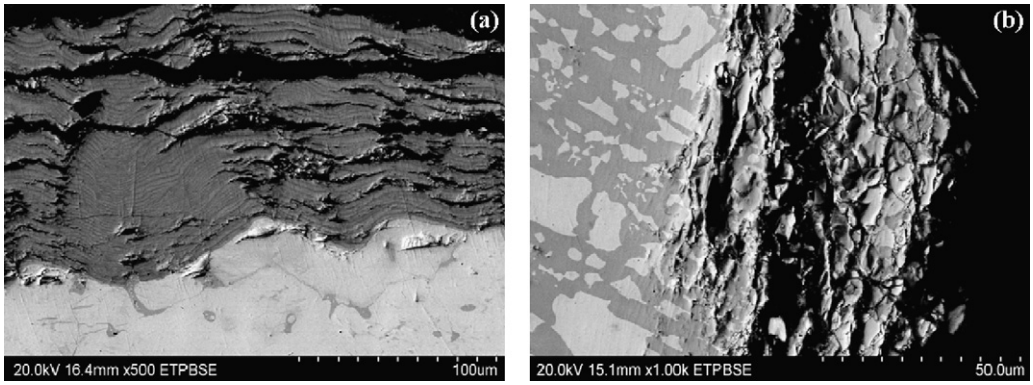

Fig. 10. BSE images of the metal–oxide interface after 24 h of exposure at 900 °C (a) 15Cr alloy and (b) 30Cr alloy.

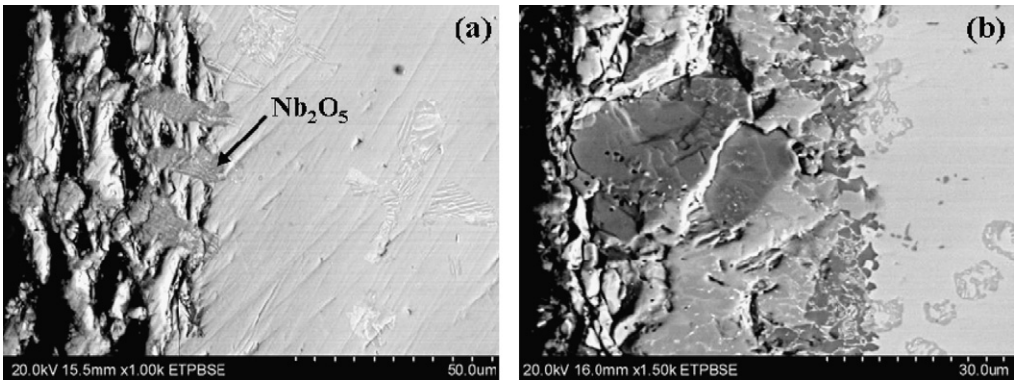

Fig. 11. BSE images of the metal–oxide interface of alloy 30Cr after exposure at 1300 °C for (a) 8 h and (b) 24 h.

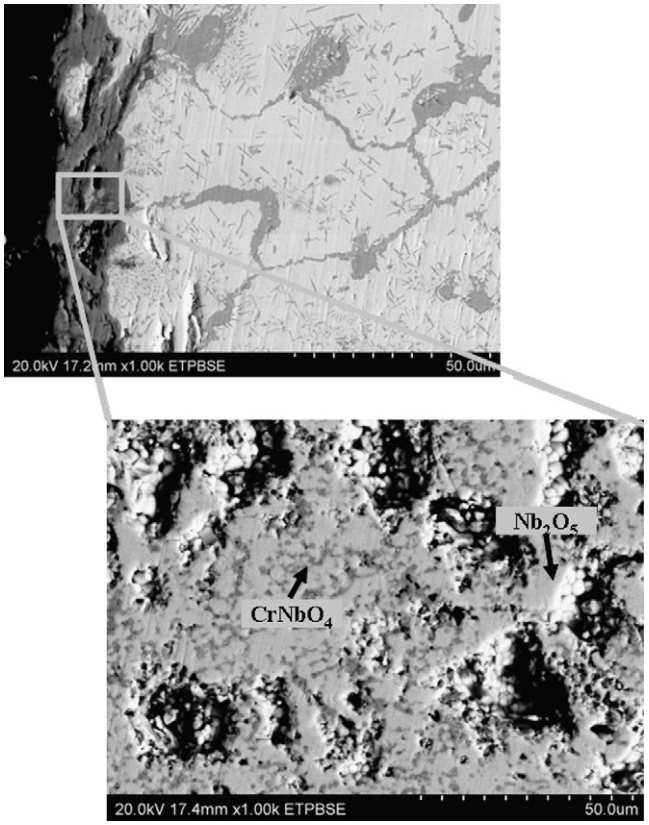

Fig. 12. BSE images of the metal–oxide interface of alloy 15Cr oxidized for 8 h at 1300 °C.

metallic phase. The poor oxidation resistance of Nb-based alloys at intermediate temperatures caused by internal oxidation and microcrack formation has been previously reported by Bewlay et al. [6], Chan [11], and Geng et al. [13,29].

The oxide–metal interface images of sample 30Cr oxidized at 1300 °C for 8 h and 24 h are presented in Fig. 11. The oxide formed is not continuous around the edge the first 8 h, showing the preferential oxidation of the solid solution phase to form Nb_2O_5 which causes the formation of cracks parallel to the surface in the intermetallic regions. Exposure for 24 h results in the formation of a thicker and smoother oxide layer, measurement of a general area of the oxide scale indicates $CrNbO_4$ is the main constituent, which is in accordance to the XRD results obtained (Fig. 8).

Fig. 12 presents a SEM micrograph showing the metal–oxide interface of 15Cr sample after oxidation at 1300 °C for 8 h. The EDS elemental analysis and BSE contrast were used to identify the composition of the oxidation products which are a mixture of Nb_2O_5, $CrNbO_4$, and irregular large pores. The oxide scale of 15Cr alloy which shows the largest mass gain is porous while scale of the alloy 30Cr presenting the lowest gain is significantly denser.

4. Conclusions

Alloy microstructure consists of Nb solid solution phase regions surrounded by a network of the $NbCr_2$ Laves phase. The amount of intermetallic phase is related to the amount of Cr content.

The oxidation behavior of the alloys is controlled by the volume fraction of intermetallic phase. Preferential attack of the Nb solid solution phase was observed in all the oxidized alloys. As temperature increases there is a change in the oxidation kinetics of alloys containing 25% and 30% of Cr from linear at 900 °C to parabolic at 1300 °C.

The oxidation kinetics follows a parabolic behavior at 1300 °C for all the analyzed alloys; the time at which the oxidation rate stabilizes is composition dependent. The addition of 30% of Cr resulted in the significant reduction of the parabolic oxidation rate.

The metal–oxide interface analysis of sample containing 30% Cr shows the preferential oxidation of the solid solution phase to form Nb_2O_5 during the first 8 h at 1300 °C. Exposure for 24 h results in the formation of a thicker and denser oxide layer composed mainly of $CrNbO_4$.

Alloys containing lower Cr concentrations exhibit better oxidation resistance than alloys with higher Cr at 900 °C; the unsatisfactory oxidation behavior of 25Cr and 30Cr alloys appears to be related to microcrack formation at the alloy perimeter.

The oxidation products of the alloys are a mixture of $CrNbO_4$, and Nb_2O_5. As the Cr concentration increases the intensity of the Nb_2O_5 peaks decreases; $CrNbO_4$ is the predominant oxide in sample containing 30% of Cr. The ratio $CrNbO_4/Nb_2O_5$ controls the morphology of the oxides formed and the spallation process.

Acknowledgements

This research has been sponsored by the National Energy Technology Laboratory of the U.S. Department of Energy, Project Number DE-FG26-05NT42491. Dr. Patricia Rawls is the program manager.

References

[1] M. Nedyakha, V.G. Chernyi, Fiziko Khimicheskaya Mekhanika Materialov 2 (6) (1966) 646–648.
[2] K.S. Chan, Oxid. Met. 61 (2004) 165–194.
[3] R.A. Perkins, K.T. Chang, G.H. Meier, R. Miller, in: T. Grobstein, J. Doychak (Eds.), Oxidation of High Temperature Intermetallics, TMS, Warrendale, 1988, pp. 157–169.
[4] J. Doychak, M.G. Hebsur, Oxid. Met. 36 (1) (1991) 113–141.
[5] B.P. Bewlay, M.R. Jackson, J.C. Zhao, P.R. Subramanian, M.G. Mendiratta, J.J. Lewandowski, MRS Bull. (September) (2003) 646–653.
[6] B.P. Bewlay, M.R. Jackson, J.C. Zhao, P.R. Subramanian, Metall. Trans. A 34 (2003) 2043–2052.
[7] P.R. Subramanian, M.G. Mendiratta, D.M. Dimiduk, M.A. Stucke, Mater. Sci. Eng. A 239 (1997) 1–13.
[8] B. Bewlay, M. Jackson, H. Lipsitt, Metall. Trans. A 27 (1996) 3801–3808.
[9] J. Geng, P. Tsakiropoulos, G. Shao, Mater. Sci. Eng. A 441 (2006) 26–38.
[10] P.R. Subramanian, M.G. Mendiratta, D.M. Dimiduk, JOM 48 (1) (1996) 33–38.
[11] K.S. Chan, Metall. Mater. Trans. A 35 (2004) 589.
[12] V. Behrani, A.J. Thom, M.J. Kramer, M. Akinc, Intermetallics 14 (2006) 24–32.
[13] J. Geng, P. Tsakiropoulos, Intermetallics 15 (2007) 382–395.
[14] C.L. Ma, J.G. Li, Y. Tan, R. Tnaka, S. Hanada, Mater. Sci. Eng. A 384 (2004) 377–384.
[15] T. Murakami, S. Sasaki, K. Ichikawa, A. Kitahara, Intermetallics 9 (2001) 629–635.
[16] E.S. Menon, M.G. Mendiratta, D.M. Dimiduk, Proceedings of the International Symposium Niobium, Orlando, FL, USA, 2001, pp. 121–145.
[17] M. Yoshida, T. Takasugi, Mater. Sci. Eng. A 262 (1999) 107–114.
[18] H. Okaniwa, D. Shindo, M. Yoshida, T. Takasugi, Acta Mater. 47 (6) (1999) 1897–1992.
[19] M. Yoshida, T. Takasugi, Mater. Sci. Eng. A 224 (1997) 69–76.
[20] P. Kakarlapudi, S. Varma, PFAM XV Proceedings, 2006, pp. 131–139.
[21] B. Portillo, P. Kakarlapudi, S.K. Varma, JOM 59 (6) (2007) 46–49.
[22] G. Wang, B. Gleeson, D.L. Douglass, Oxid. Met. 35 (5/6) (1991) 333–348.
[23] F. Gesmundo, F. Viani, Y. Niu, D.L. Douglass, Oxid. Met. 39 (3/4) (1993) 197–209.
[24] F. Gesmundo, F. Viani, Y. Niu, D.L. Douglass, Oxid. Met. 40 (3/4) (1993) 373–393.
[25] J. English, in: H. Baker (Ed.), ASM Handbook, vol. 3, Materials Park, Ohio, 1999, pp. 3–47.
[26] PandatTM 7.0, Multi-component Phase Equilibrium Calculation Software, Computherm LLC, Madison, WI, 2007.
[27] J. Lambert, M. Schussler, ASM Handbook. Metallography and Microstructures, vol. 9, Materials Park, Ohio, 1998, p. 440.
[28] W.F. Gaze, T.C. Totemeier (Eds.), Smithells Metals Reference Book, 8th ed., Elsevier Butterworth-Heinemann, 2004.
[29] J. Geng, P. Tsakiropoulos, Intermetallics 15 (2007) 270–281.